

# Distributed current sensing technology for protection and fault location applications in high-voltage direct current networks

Dimitrios Tzelepis<sup>1</sup> ✉, Adam Dysko<sup>1</sup>, Campbell Booth<sup>1</sup>, Grzegorz Fusiek<sup>1</sup>, Pawel Niewczas<sup>1</sup>, Tzu Chief Peng<sup>1</sup>

<sup>1</sup>Department of Electronic and Electrical Engineering, University of Strathclyde, Glasgow, UK

✉ E-mail: dimitrios.tzelepis@strath.ac.uk

eISSN 2051-3305  
Received on 3rd May 2018  
Accepted on 11th June 2018  
doi: 10.1049/joe.2018.0219  
www.ietdl.org

**Abstract:** This study presents a novel concept for a distributed current optical sensing network, suitable for protection and fault location applications in high-voltage multi-terminal direct current (HV-MTDC) networks. By utilising hybrid fibre Bragg grating-based voltage and current sensors, a network of current measuring devices can be realised which can be installed on an HV-MTDC network. Such distributed optical sensing network forms a basis for the proposed 'single-ended differential protection' scheme. The sensing network is also a very powerful tool to implement a travelling-wave-based fault locator on hybrid transmission lines, including multiple segments of cables and overhead lines. The proposed approach facilitates a unique technical solution for both fast and discriminative DC protection, and accurate fault location, and thus, could significantly accelerate the practical feasibility of HV-MTDC grids. Transient simulation-based studies presented in the paper demonstrate that by adopting such sensing technology, stability, sensitivity, speed of operation and accuracy of the proposed (and potentially others) protection and fault location schemes can be enhanced. Finally, the practical feasibility and performance of the current optical sensing system has been assessed through hardware-in-the-loop testing.

## 1 Introduction

Power transmission based on high-voltage direct current (HVDC) networks is expected to be the favoured technology for massive integration of renewable energy sources and the realisation of European and Asian supergrids [1, 2]. DC-side faults are the greatest challenge when it comes to the realisation of HVDC-based grids, due to the fact that large inrush currents escalating over a short period of time [3].

After the occurrence of a DC-side fault on an HVDC transmission system, dedicated protection schemes are expected to minimise its adverse effects, by initiating fault-clearing actions such as selective tripping of circuit breakers. Following the fast and successful fault clearance, the next important action is the accurate calculation of its distance with regards to feeder's length. This is of major importance as it will permit faster system restoration, diminish the power outage time, and therefore enhance the overall reliability of the system.

Distributed sensing in power systems is an advanced, cutting-edge technology (with numerous operational, technical and economic benefits) which aims to accelerate power system protection and control applications [4–11]. In this paper, the work conducted in [4, 5] is further demonstrated to highlight the technical merits when adopted for protection and fault location applications in HVDC networks.

## 2 Modelling

For the studies presented in this paper, a five terminal multi-terminal direct current (MTDC) grid (illustrated in Fig. 1) has been developed in Matlab/Simulink. The system architecture has been adopted from the Twenties Project case study on DC grids. There are five 400-level, modular multilevel converters operating at  $\pm 400$  kV (in symmetric monopole configuration), hybrid circuit breakers (HbCBs), and current limiting inductors at each transmission line end.

The MTDC network includes uniform feeders but also hybrid feeders comprising of both overhead lines (OHLs) and underground cables (UGCs). It should be noted that feeders 1, 3 and 5 will be utilised for demonstrating the proposed HVDC

protection scheme while feeders 3 and 4 will be used to demonstrate a fault location scheme. On each uniform feeders (i.e. feeders 1, 2 and 5), optical sensors are installed to accurately measure DC current every 30 km including the terminals. On hybrid feeders optical sensors are installed at junctions and feeder terminals. The measurements are captured and processed at each line terminal ('relay and fault locator station'). Transmission lines have been modelled by adopting distributed parameter model, while for the DC breaker a hybrid design by ABB [12] has been considered. The parameters of the AC/DC network components are described in detail in Table 1 and line parameters in Table 2.

## 3 Single-ended differential protection scheme

### 3.1 Protection algorithm

The single-ended differential protection algorithm is illustrated using a flowchart in Fig. 2 [4].

Using the measurements of two consecutive sensors, the algorithm starts by calculating a series of differential currents given as

$$\Delta i_{(f)}(t) = i_{s(f)}(t - \Delta t) - i_{s(f+1)}(t) \quad (1)$$

where  $\Delta i_{(f)}(t)$  is the  $f$ th differential current derived using the currents  $i_{s(f)}$ ,  $i_{s(f+1)}$  measured at two adjacent sensors  $f$  and  $f+1$ , respectively ( $f = 1, 2, \dots, n-1$ ) and  $\Delta t$  the amount of time compensation due to propagation delays.

The protection logic has three stages. The first stage (Stage A) is a comparison of differential current  $\Delta i_{(f)}(t)$  with a predefined threshold value  $I_{TH}$ . When the threshold  $I_{TH}$  is exceeded for a differential current  $\Delta i_{(f)}$ , the protection algorithm will inspect the historical data of  $di_{s(f)}/dt$  and  $di_{s(f+1)}/dt$  using a short-time window  $\Delta t_w = 0.2$  ms. If any of the historical values of the derivatives  $di_{s(f)}/dt(t - \Delta t_w)$  or  $di_{s(f+1)}/dt(t - \Delta t_w)$  exceed a predefined threshold  $di/dt_{TH}$ , the criterion for Stage B is fulfilled. This stage will ensure stability of protection to any kind of short disturbance. The final stage (Stage C) is included to ensure that the operation of the protection scheme does not originate from any sensor failure. If

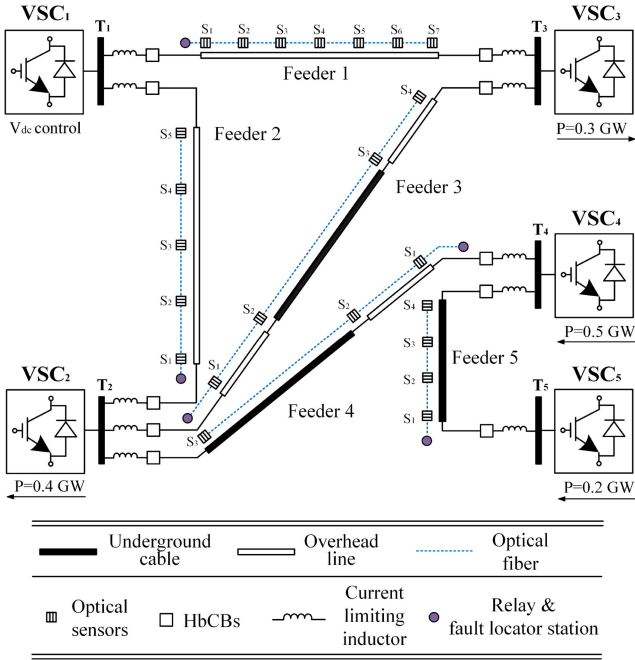


Fig. 1 Five-terminal MTDC grid

Table 1 MTDC network parameters

| Parameter                   | Value |
|-----------------------------|-------|
| DC voltage, kV              | ±400  |
| DC inductor, mH             | 150   |
| AC frequency, Hz            | 50    |
| AC short-circuit level, GVA | 40    |
| AC voltage, kV              | 400   |

no sensor failure is detected, Stage C initiates a tripping signal to the corresponding CB.

The resulting key advantages of the proposed single-ended differential protection include high speed of operation, enhanced reliability and superior stability. Detailed evaluation of the method can be found in [4].

### 3.2 Simulation results

The protection performance of the proposed scheme has been tested for numerous faults along the MTDC case study grid (faults have been applied on feeders 1, 2 and 5). It should be noted that the protection scheme is based on a sampling rate of 5 kHz.

Fig. 3 illustrates the protection response to an internal fault (initiated at  $t = 100$  ms) occurring at 50 km (from terminal  $T_1$ ) on feeder 1. This fault is practically located between sensors  $S_2$  and  $S_3$ . As such, the differential current  $I_{diff(S_2-S_3)}$  calculated from the measurements of sensors  $S_2$  and  $S_3$  is increasing rapidly (Fig. 3a), exceeding the protection threshold, and hence, fulfilling Stage A. Fig. 3b demonstrates that prior to the fault detection the rate of change  $di_{DC}/dt$  for both currents (sensors  $S_2$  and  $S_3$ ) is non-zero which indicates the fulfilment of Stage B. A tripping signal is initiated by the third criterion (Stage C); however, it is not depicted here due to space limitations. The fault current interruption is depicted in Figs. 3c and d for both ends of feeder 1.

The summarised results are presented in Tables 3 and 4 for pole-to-pole and pole-to-ground faults (with ground fault resistances of up to 300  $\Omega$ ), respectively. It can be demonstrated that in all cases only the required breakers operate, proving high selectivity of the scheme.

## 4 Enhanced fault location for hybrid feeders

Fault location in the case of hybrid feeders is not a straight-forward task and hence travelling wave-based methods cannot be directly

Table 2 Lengths of OHLs and UGCs included in MTDC case study grid

|       |   |
|-------|---|
| HTM-1 | OHL: 180 km                             |
| HTM-2 | OHL: 120 km                             |
| HTM-3 | OHL-a: 65 km, UGC: 180 km, OHL-b: 35 km |
| HTM-4 | UGC: 50 km, OHL: 130 km                 |
| HTM-5 | UGC: 90 km                              |

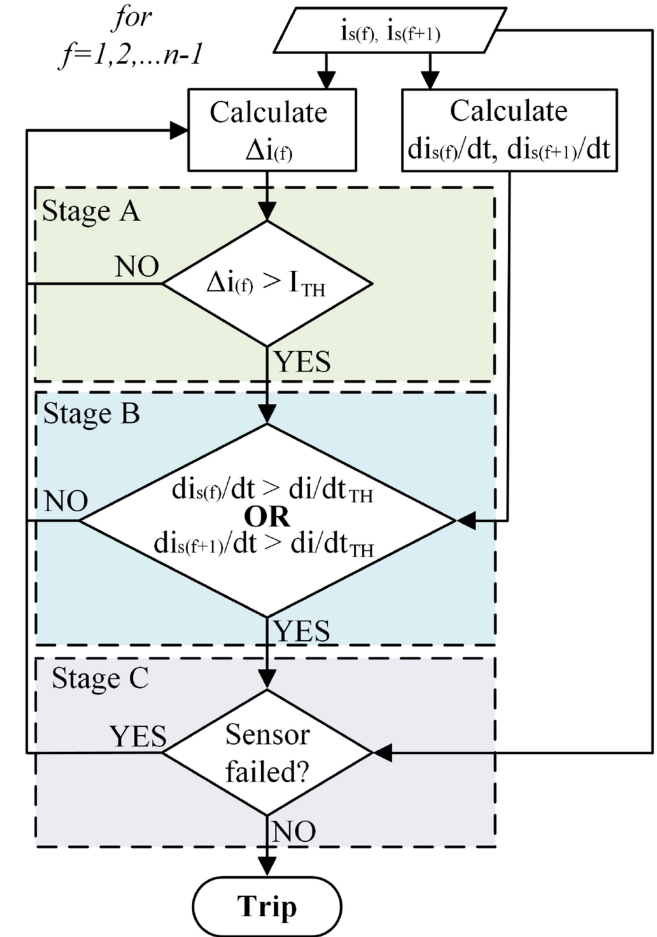


Fig. 2 Protection algorithm of single-ended differential protection scheme

applied. This arises from the fact that in such feeders, the speed of electromagnetic wave propagation is not uniform, additional reflections/refractions are generated at the junction points, and there is an increased difficulty in recognising the faulted segment. The fault location scheme presented in this paper [5] utilises the principle of travelling waves applied to a series of captured waveforms acquired from current sensors installed along hybrid feeders (see feeders 3 and 4 in Fig. 1).

### 4.1 Fault location algorithm

The proposed fault location algorithm consists of three stages as illustrated in Fig. 4.

The first stage (Stage A) of the algorithm identifies the faulted segment. This is implemented by calculating the differential current  $\Delta i_{(f)}$  for every pair of adjacent sensors (similarly to (1)). When a fault occurs between two sensors, the differential current  $\Delta i_{(f)}$  calculated from measurements acquired from those sensors reaches much higher level than the current captured from any other adjacent pair (this was also demonstrated in Fig. 3a). As such, by identifying the highest differential current, the faulted segment is identified. At this point the algorithm will produce two outputs:  $S_{up}$  and  $S_{dn}$  for the sensors located upstream downstream to the fault, respectively.

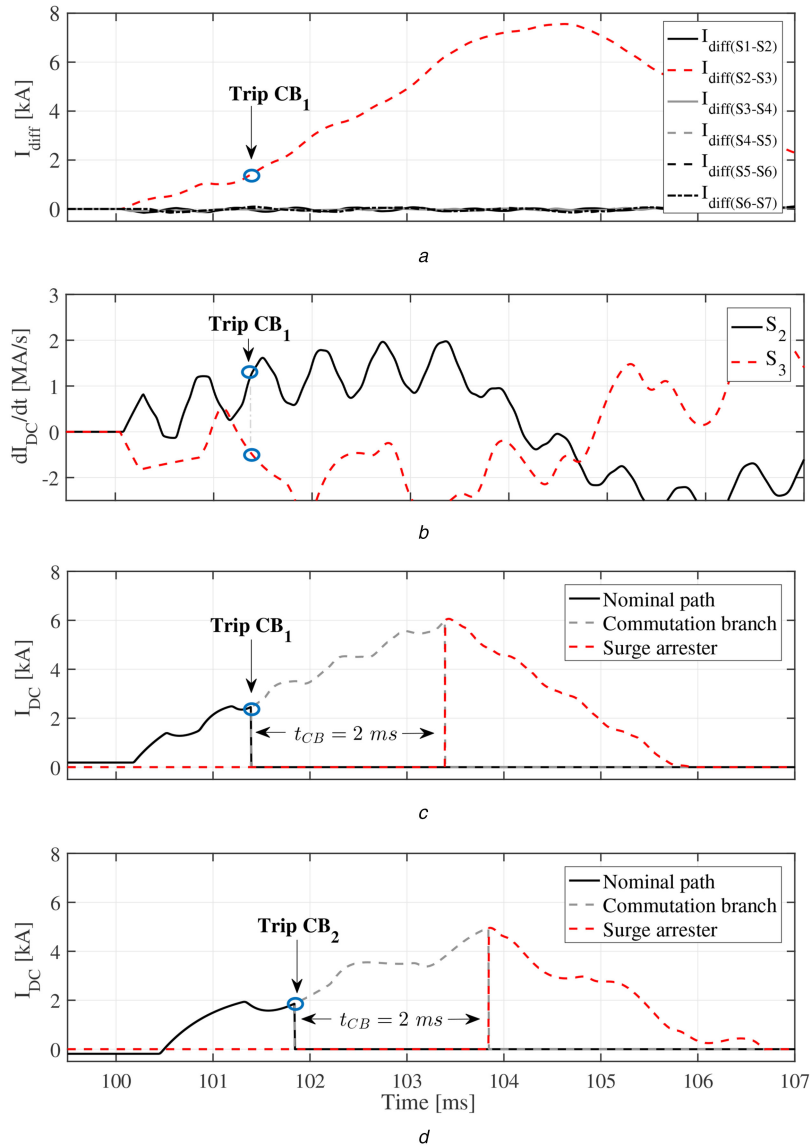


**Fig. 3** Illustration of pole-to-pole fault at feeder 1

(a) Differential current  $\Delta i_{ij}(t)$ , (b) Rate of change of DC current, (c) Fault current interruption in HbCB, (d) Experimental setup diagram

**Table 3** Protection performance results for pole-to-pole faults

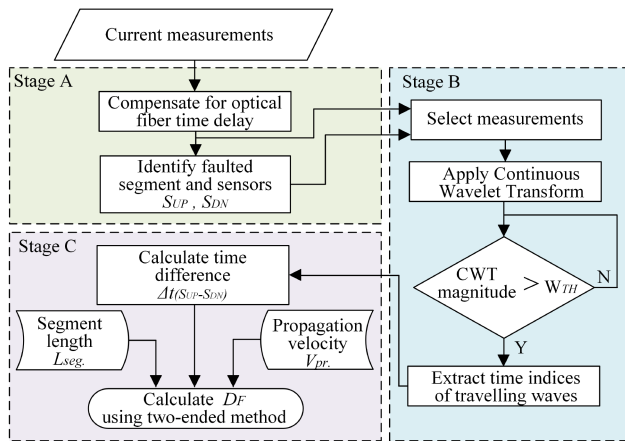
| Line | Distance, km | Breakers operated                  | Sending end      |                     | Receiving end    |                     |
|------|--------------|------------------------------------|------------------|---------------------|------------------|---------------------|
|      |              |                                    | CB trip time, ms | CB max. current, kA | CB trip time, ms | CB max. current, kA |
| 1    | 1            | CB <sub>1</sub> , CB <sub>2</sub>  | 1.329            | 7.45                | 2.075            | 4.07                |
|      | 90           | CB <sub>1</sub> , CB <sub>2</sub>  | 1.525            | 5.12                | 1.675            | 5.28                |
|      | 120          | CB <sub>1</sub> , CB <sub>2</sub>  | 1.677            | 5.41                | 1.525            | 5.82                |
|      | 179          | CB <sub>1</sub> , CB <sub>2</sub>  | 2.074            | 4.44                | 1.331            | 7.07                |
| 2    | 1            | CB <sub>3</sub> , CB <sub>4</sub>  | 1.327            | 7.49                | 1.775            | 5.17                |
|      | 25           | CB <sub>3</sub> , CB <sub>4</sub>  | 1.280            | 6.47                | 1.730            | 5.00                |
|      | 60           | CB <sub>3</sub> , CB <sub>4</sub>  | 1.373            | 5.97                | 1.524            | 5.81                |
|      | 119          | CB <sub>3</sub> , CB <sub>4</sub>  | 1.774            | 5.56                | 1.326            | 7.06                |
| 5    | 1            | CB <sub>9</sub> , CB <sub>10</sub> | 1.325            | 7.33                | 1.630            | 5.20                |
|      | 45           | CB <sub>9</sub> , CB <sub>10</sub> | 1.376            | 6.18                | 1.374            | 5.73                |
|      | 89           | CB <sub>9</sub> , CB <sub>10</sub> | 1.631            | 5.64                | 1.330            | 6.98                |

Since the faulted segment has been identified in Stage A, post-fault current measurements corresponding to sensors  $S_{up}$  and  $S_{dn}$  are utilised at the next stage (Stage B). These measurements are used to calculate the precise time of travelling wave arrival at faulted segment terminals (where the sensors  $S_{up}$  and  $S_{dn}$  are located). The wave detection is implemented by applying continuous wavelet transform (CWT) on the available current

measurements. The wavelet transform of a function  $i(t)$  can be expressed as the integral of the product of  $i(t)$  and the daughter wavelet  $\Psi_{a,b}^*(t)$  given as

**Table 4** Protection performance results for pole-to-ground faults

| Line | Distance, km | Breakers operated                  | Sending end      |                     | Receiving end    |                     |
|------|--------------|------------------------------------|------------------|---------------------|------------------|---------------------|
|      |              |                                    | CB trip time, ms | CB max. current, kA | CB trip time, ms | CB max. current, kA |
| 1    | 1            | CB <sub>1</sub> , CB <sub>2</sub>  | 1.382            | 1.65                | 2.125            | 1.05                |
| —    | 90           | CB <sub>1</sub> , CB <sub>2</sub>  | 1.565            | 1.40                | 1.715            | 1.12                |
| —    | 120          | CB <sub>1</sub> , CB <sub>2</sub>  | 1.714            | 1.42                | 1.567            | 1.19                |
| —    | 179          | CB <sub>1</sub> , CB <sub>2</sub>  | 2.128            | 1.38                | 1.380            | 1.43                |
| 2    | 1            | CB <sub>3</sub> , CB <sub>4</sub>  | 1.377            | 2.12                | 1.820            | 0.98                |
| —    | 25           | CB <sub>3</sub> , CB <sub>4</sub>  | 1.330            | 2.03                | 1.780            | 1.03                |
| —    | 60           | CB <sub>3</sub> , CB <sub>4</sub>  | 1.420            | 1.84                | 1.566            | 1.04                |
| —    | 119          | CB <sub>3</sub> , CB <sub>4</sub>  | 1.830            | 1.75                | 1.381            | 1.22                |
| 5    | 1            | CB <sub>9</sub> , CB <sub>10</sub> | 1.400            | 0.81                | 1.700            | 1.08                |
| —    | 45           | CB <sub>9</sub> , CB <sub>10</sub> | 1.415            | 0.74                | 1.414            | 1.13                |
| —    | 89           | CB <sub>9</sub> , CB <sub>10</sub> | 1.680            | 0.86                | 1.383            | 1.25                |

**Fig. 4** Protection algorithm of fault location scheme

$$WT_{\Psi} i(t) = \int_{-\infty}^{\infty} i(t) \underbrace{\frac{1}{\sqrt{a}} \Psi\left(\frac{t-b}{a}\right)}_{\text{daughter wavelet } \Psi_{a,b}^*(t)} dt \quad (2)$$

The daughter wavelet  $\Psi_{a,b}^*(t)$  is a scaled and shifted version of the mother wavelet  $\Psi_{a,b}(t)$ . Scaling is implemented by which is the binary dilation (also known as scaling factor) and shifted by  $b$  which is the binary position (also known as shifting or translation). Finally, Stage B will produce two outputs:  $t_{sup}$  and  $t_{dn}$  which correspond to the time index of the initial travelling wave at the faulted segment terminals.

In Stage C of the proposed algorithm, the actual fault location  $D_F$  of the faulted segment is calculated by adopting the conventional, two-ended fault location approach given as

$$D_F = \frac{L_{seg} - \Delta t_{(S_{up}-S_{dn})} \cdot v_{prop}}{2} \quad (3)$$

where  $\Delta t_{(S_{up}-S_{dn})}$  is the time difference of the initial travelling waves at sensing locations  $S_{up}$  and  $S_{dn}$ , and  $v_{prop}$  is the propagation velocity of the faulted segment (the propagation velocity has been calculated according to the conductor geometry).

#### 4.2 Simulation results

In order to validate the performance of the proposed scheme, pole-to-pole and pole-to-ground faults have been applied on feeders 3 and 4 (see Fig. 1) at various distances at all segments. Since the accuracy of travelling wave-based techniques depend on sampling frequency, for the studies presented in this paper a sampling rate of 135 kHz has been assumed. This frequency corresponds to the resonant frequency of optical sensors and the signal acquisition at this rate can be practically achieved by employing arrayed

waveguide grating interrogators [13]. The values of fault location estimation error have been reported as

$$\text{error, \%} = \frac{D_F - A_{DF}}{L_{f-seg}} \cdot 100\% \quad (4)$$

where  $D_F$  is the calculated fault distance,  $A_{DF}$  is the actual fault distance and  $L_{f-seg}$  the total length of the faulted segment.

The results are presented in Tables 5 and 6 for pole-to-pole and pole-to-ground faults, respectively. The average, minimum and maximum errors observed for pole-to-pole faults correspond to 0:3644%, 0:0012% and 1:4625%, respectively. For pole-to-ground faults, these errors correspond to 0:3955%, 0:0390% and 1:3214%, respectively. It can be also seen that the faulted segment has been identified correctly in 100% of the cases for both types of faults (see ‘Reported sensors’ column in Tables 5 and 6).

The impact of noise in measurements, mother wavelet, scaling factor and network components on the accuracy of the proposed fault location scheme are exhaustively analysed and reported in [5].

## 5 Hardware validation of optical sensing technology

### 5.1 Experimental setup

In order to prove the principle of the new protection and fault location scheme, an experimental set-up has been arranged as shown in Fig. 5 (the actual laboratory experiment is shown in Fig. 6). For the realisation of such an experimental set-up the following key components were required:

- Four fibre Bragg grating optical sensors
- Four transient voltage suppression diodes
- Optical fibre
- SmartScan interrogator
- PXIe-8106 controller (National Instruments)
- PXIe-6259 data acquisition card (National Instruments)
- Pre-simulated DC fault currents
- PC

For the practical implementation of the proposed schemes, pre-simulated fault currents at corresponding four sensing locations have been generated and stored locally to a PC. For the proposed single-ended differential protection scheme, the model of feeder 5 has been utilised with one fault placed at 50 km (see Fig. 5a). For testing the proposed fault location scheme, the model of feeder 3 has been utilised (see Fig. 5b). The pre-simulated fault currents were used to generate replica voltage traces using the data acquisition card. Such voltage waveforms were physically injected to optical sensors and the corresponding data were captured at 5 kHz from the optical interrogator. The sampled data were then stored on a PC for post-processing. Further technical details with

**Table 5** Segment identification and fault location results for pole-to-pole faults

| Feeder | Segment | Fault distance, km | Reported sensors |          | Reported fault location, km | Error, % |
|--------|---------|--------------------|------------------|----------|-----------------------------|----------|
|        |         |                    | $S_{UP}$         | $S_{DN}$ |                             |          |
| 3      | OHL-a   | 12.4               | $S_1$            | $S_2$    | 11.7669                     | -0.9740  |
| 3      | OHL-a   | 35.0               | $S_1$            | $S_2$    | 35.7736                     | 1.1902   |
| 3      | OHL-a   | 42.0               | $S_1$            | $S_2$    | 42.3209                     | 0.4937   |
| 3      | OHL-a   | 50.1               | $S_2$            | $S_3$    | 51.0506                     | 1.4625   |
| 3      | OHL-a   | 57.3               | $S_2$            | $S_3$    | 57.5979                     | 0.4583   |
| 3      | UGC     | 10.0               | $S_2$            | $S_3$    | 9.6516                      | -0.1936  |
| 3      | UGC     | 39.7               | $S_2$            | $S_3$    | 39.9929                     | 0.1627   |
| 3      | UGC     | 56.7               | $S_2$            | $S_3$    | 56.8493                     | 0.0829   |
| 3      | UGC     | 95.0               | $S_2$            | $S_3$    | 95.0569                     | 0.0316   |
| 3      | UGC     | 100.0              | $S_2$            | $S_3$    | 99.5519                     | -0.2489  |
| 3      | UGC     | 103.0              | $S_2$            | $S_3$    | 102.9232                    | -0.0427  |
| 3      | UGC     | 161.2              | $S_2$            | $S_3$    | 161.3584                    | 0.0880   |
| 3      | UGC     | 173.0              | $S_3$            | $S_4$    | 172.5959                    | -0.2245  |
| 3      | OHL-b   | 26.7               | $S_3$            | $S_4$    | 26.6210                     | -0.2256  |
| 3      | OHL-b   | 30.0               | $S_3$            | $S_4$    | 29.9337                     | -0.1893  |
| 3      | OHL-b   | 33.7               | $S_3$            | $S_4$    | 33.8682                     | 0.4806   |
| 4      | UGC     | 3.8                | $S_1$            | $S_2$    | 3.6487                      | -0.3027  |
| 4      | UGC     | 13.2               | $S_1$            | $S_2$    | 13.2006                     | 0.0012   |
| 4      | UGC     | 29.10              | $S_1$            | $S_2$    | 29.4950                     | 0.7900   |
| 4      | UGC     | 46.6               | $S_1$            | $S_2$    | 46.3513                     | -0.4973  |
| 4      | OHL     | 29.0               | $S_2$            | $S_3$    | 28.9899                     | -0.0077  |
| 4      | OHL     | 53.5               | $S_2$            | $S_3$    | 52.9966                     | -0.3872  |
| 4      | OHL     | 74.0               | $S_2$            | $S_3$    | 73.7297                     | -0.2079  |
| 4      | OHL     | 110.2              | $S_2$            | $S_3$    | 109.7398                    | -0.3540  |
| 4      | OHL     | 125.0              | $S_2$            | $S_3$    | 125.0168                    | 0.0129   |

regards to the design, operation and installation of optical sensors can be found in [4, 5].

## 5.2 Experimental results

The measured response of the optical sensors and the protection system to fault at feeder 5 is illustrated in Fig. 7. The recorded DC voltages were used to calculate the differential voltage  $\Delta v$  (corresponding to differential current  $\Delta i_f$ ) described in (1) which is depicted in Fig. 7a. It is evident that the differential voltage between sensors  $S_1$  and  $S_2$  reaches high values which can be easily detected by a voltage threshold. The corresponding rate of change of voltage  $dV_{dc}/dt$  of the measurements captured from sensors  $S_1$  and  $S_2$  stay high within a 0.2 ms time window. The entire response of the system is of great resemblance to simulation-based results and hence the protection scheme can be considered practically feasible.

The experimental results related to the proposed fault location scheme (i.e. experimental arrangement shown in Fig. 5b) are summarised in Table 7, where they are also compared with the simulation-based results. Due to the reduced sampling rate (i.e. 5 kHz), the resulting accuracy of the experimentally calculated fault location is notably lower. The sampling frequency has a significant impact on the CWT and the extraction of time difference  $\Delta t(S_{up} - S_{dn})$  which is utilised in (3) for the calculation of fault distance. This can be further justified from the values of time difference  $\Delta t(S_{up} - S_{dn})$  exacted for each fault case, as shown in Table 7. With regards to faulted segment, the reported sensors  $S_{up}$  and  $S_{dn}$  demonstrate that it has been identified correctly at all cases. It should be noted that the resulting diminished accuracy is due to the reduced sampling rate, determined by the available interrogation system. However, the assumed sampling frequency of 135 kHz is practically achievable with other, commercially available equipment.

## 5.3 Discussion

It has been demonstrated within this paper that optical sensing technology can further enhance the overall performance of protection and fault location applications. This has been demonstrated for HVDC applications, however such technology has been previously utilised in [6–10] for protection and control applications in AC systems. The protection, control and fault location schemes have been realised by the employment of optical current and voltage sensors. Such sensors have been designed and manufactured based on magneto-optical constructions based on fibre coils, extrinsic magnetostrictive materials bonded to fibre strain sensors.

In this paper, optical sensors have been used for two different applications namely protection and fault location. The schemes developed for these two applications have been designed and tested separately. For example, for the proposed protection scheme, the sensors have been interrogated at a sampling rate of 5 kHz, while for the fault location scheme a sampling rate of 135 kHz has been assumed. The fundamental difference of these two applications is that the protection needs to be run in real time while for distance to fault estimation off-line computations can be used. Therefore, lower sampling rate (i.e. 5 kHz) is adequate to permit computational efficiency and high-speed operation of the protection module. However, for fault location applications higher sampling rates have to be used in order to guarantee sufficient fault location accuracy. Since the two proposed schemes utilise the same sensing architecture, there is no reason why they could not coexist sharing the same fundamental sensing and interrogation hardware, and forming an integrated protection and fault location system. So long as the fault generated waveforms are captured at adequate sampling rate (i.e. in excess of 100 kHz) both protective and fault locating functions could be performed independently in their respective operating time frames. This would satisfy both, the need for high speed of protection operation and high accuracy of fault location. For example, a real-time calculation with operating frame

**Table 6** Segment identification and fault location results for pole-to-ground faults ( $R_f = 500 \Omega$ )

| Feeder | Segment | Fault distance, km | Reported sensors |          | Reported fault location, km | Error, % |
|--------|---------|--------------------|------------------|----------|-----------------------------|----------|
|        |         |                    | $S_{UP}$         | $S_{DN}$ |                             |          |
| 3      | OHL-a   | 8.1                | $S_1$            | $S_2$    | 8.4933                      | 0.6051   |
| 3      | OHL-a   | 23.8               | $S_1$            | $S_2$    | 24.5979                     | 1.2276   |
| 3      | OHL-a   | 35.6               | $S_1$            | $S_2$    | 35.7736                     | 0.2671   |
| 3      | OHL-a   | 46.5               | $S_1$            | $S_2$    | 46.6858                     | 0.2858   |
| 3      | OHL-a   | 55.5               | $S_1$            | $S_2$    | 55.4155                     | -0.1300  |
| 3      | UGC     | 8.8                | $S_2$            | $S_3$    | 8.5278                      | -0.1512  |
| 3      | UGC     | 12                 | $S_2$            | $S_3$    | 11.8991                     | -0.0561  |
| 3      | UGC     | 33                 | $S_2$            | $S_3$    | 33.2504                     | 0.1391   |
| 3      | UGC     | 56.4               | $S_2$            | $S_3$    | 56.2874                     | -0.0626  |
| 3      | UGC     | 100                | $S_2$            | $S_3$    | 100.1138                    | 0.0632   |
| 3      | UGC     | 144.3              | $S_2$            | $S_3$    | 144.5021                    | 0.1123   |
| 3      | UGC     | 156                | $S_2$            | $S_3$    | 155.7396                    | -0.1447  |
| 3      | UGC     | 165.7              | $S_2$            | $S_3$    | 165.8534                    | 0.0852   |
| 3      | UGC     | 177.5              | $S_2$            | $S_3$    | 177.6528                    | 0.0849   |
| 3      | OHL-b   | 15.2               | $S_3$            | $S_4$    | 15.3176                     | 0.3359   |
| 3      | OHL-b   | 34                 | $S_3$            | $S_4$    | 33.8682                     | -0.3765  |
| 4      | UGC     | 5.1                | $S_1$            | $S_2$    | 5.3343                      | 0.4686   |
| 4      | UGC     | 28                 | $S_1$            | $S_2$    | 28.3713                     | 0.7425   |
| 4      | UGC     | 42                 | $S_1$            | $S_2$    | 42.4182                     | 0.8364   |
| 4      | UGC     | 48.5               | $S_1$            | $S_2$    | 49.1607                     | 1.3214   |
| 4      | OHL     | 4                  | $S_2$            | $S_3$    | 2.8008                      | -0.9225  |
| 4      | OHL     | 66                 | $S_2$            | $S_3$    | 66.0912                     | 0.0702   |
| 4      | OHL     | 83.5               | $S_2$            | $S_3$    | 83.5506                     | 0.0390   |
| 4      | OHL     | 99                 | $S_2$            | $S_3$    | 98.8276                     | -0.1326  |
| 4      | OHL     | 115.7              | $S_2$            | $S_3$    | 116.2871                    | 0.4516   |

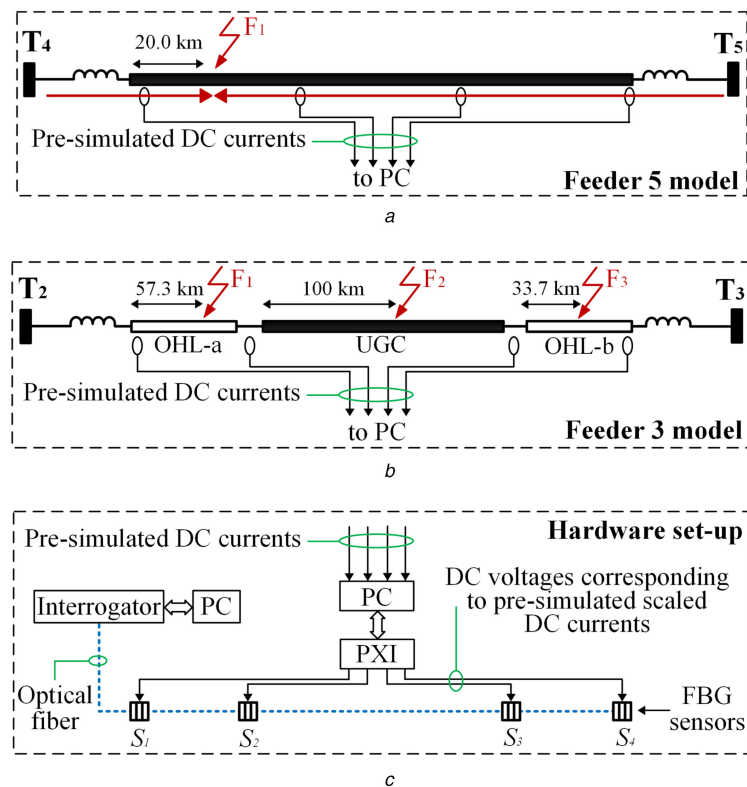


**Fig. 5** Laboratory arrangement diagram  
 (a) Feeder 5 model, (b) Feeder 3 model, (c) Optical sensing setup

rate in the range of 5 kHz (using down-sampled data) would be adequate for protection, while for fault location a non-real-time

post-fault calculation could be performed using the stored data acquired at much higher frequency. A circular memory buffer of

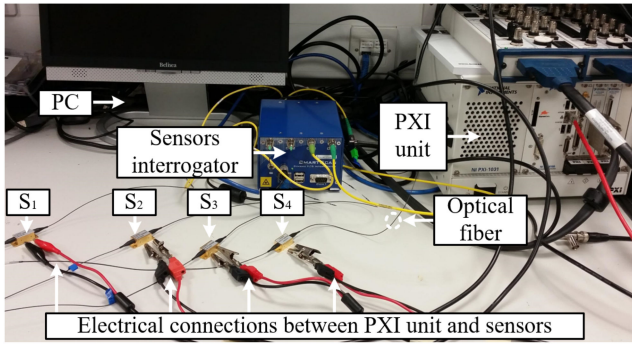


Fig. 6 Laboratory experimental arrangement

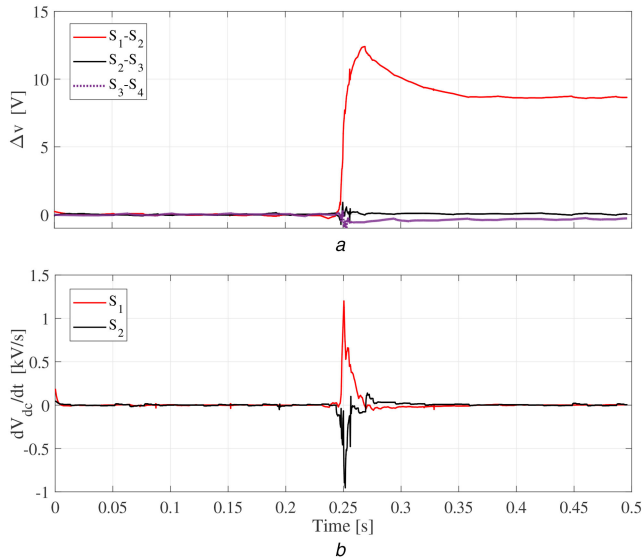


Fig. 7 Optical and protection system response for presimulated fault at feeder 5

(a) Differential voltage  $\Delta v$ , (b) Rate of change of DC voltage  $\Delta v$

Table 7 Comparison of experimental and simulations results

| Faults                                | F1         | F2         | F3         |
|---------------------------------------|------------|------------|------------|
| error, %                              |            |            |            |
| sim.                                  | 0.4583     | -0.2489    | 0.4806     |
| exp.                                  | -1.3254    | -1.3415    | 1.0652     |
| $ \Delta t_{(S_{UP}-S_{DN})} , \mu s$ |            |            |            |
| sim.                                  | 0.17037    | 0.12592    | 0.11110    |
| exp.                                  | 0.16249    | 0.10000    | 0.11250    |
| reported sensors $S_{UP} - S_{DN}$    |            |            |            |
| sim.                                  | $S_1, S_2$ | $S_2, S_3$ | $S_3, S_4$ |
| exp.                                  | $S_1, S_2$ | $S_2, S_3$ | $S_3, S_4$ |

~100 ms should provide sufficient amount of data to achieve accurate fault position estimation.

For application in electrical power systems, the key technical and economical merits of the utilised distributed sensing technology (compared to other conventional and purely electrical), arise from the fact that the sensors are completely passive and require no power supply at the sensing location. Moreover, there is no need for additional signal processing and communication equipment (i.e. micro-controllers, GPS etc.) at the location of the sensors (i.e. sensors are interrogated from a single acquisition point, where measurements can also be time stamped). These technical merits have the potential to enable reduction in the hardware and infrastructure needs (i.e. communications, low-voltage power supplies, decoders/encoders etc.) required for wide-area monitoring applications. It should also be highlighted that over the last decade the cost of optical sensors has been decreased

adequately, leading to practical realisation of cheap and high-performance transducers. Overall, due to the extensibility and centralised nature of the sensing technology, the capability of distributed sensing is undoubtedly technically beneficial, while in the long term, it can ultimately lead to reduction of operational and capital expenditure. Since measurements have been made available [14] in standardised sampled value formats (IEC 61850-9-2), it can be considered a ready-to-use technology for substation automation, and for protection and control of electrical networks (from microgrids to large transmission lines).

## 6 Conclusions

In this paper, a new single-ended differential protection scheme and a fault location scheme for hybrid feeders has been presented. Such schemes were designed for HV-MTDC networks and are based upon the principle of distributed optical sensing. The proposed protection scheme has been found to be highly sensitive, discriminative and fast both for pole-to-pole and pole-to-ground faults. With regards to fault location in hybrid feeders, the proposed travelling wave-based algorithm has been found to be capable of identifying the faulted segment, while maintaining high accuracy of the fault location estimation across a wide range of fault scenarios. The overall performance of both schemes has been assessed through transient simulation and further validated using small-scale hardware prototypes and hardware-in-the-loop testing. The potential technical and economical benefits of distributed sensing technology have been also discussed within this paper.

## 7 Acknowledgments

This work was supported by Royal Society of Edinburgh (J. M. Lessells Travel Scholarship), Synaptec Ltd j Glasgow – UK, the Innovate UK (TSB Project Number 102594) and the European Metrology Research Programme (EMRP) – ENG61. The EMRP is jointly funded by the EMRP participating countries within EURAMET and the European Union.

## 8 References

- [1] Tzelepis, D., Rousis, A.O., Dysko, A., *et al.*: 'A new fault-ride-through strategy for MTDC networks incorporating wind farms and modular multi-level converters', *Electr. Power Energy Syst.*, 2017, **92**, pp. 104–113
- [2] Hertem, D.V., Ghandhari, M.: 'Multi-terminal VSC-HVDC for the European supergrid: obstacles', *Renew. Sust. Energy Rev.*, 2010, **14**, (9), pp. 3156–3163
- [3] Tzelepis, D., Ademi, S., Vozikis, D., *et al.*: 'Impact of VSC converter topology on fault characteristics in HVDC transmission systems', IET 8th Int. Conf. Power Electronics Machines and Drives, Glasgow, UK, March 2016
- [4] Tzelepis, D., Dyko, A., Fusiek, G., *et al.*: 'Single-ended differential protection in MTDC networks using optical sensors', *IEEE Trans. Power Deliv.*, 2017, **32**, (3), pp. 1605–1615
- [5] Tzelepis, D., Fusiek, G., Dyko, A., *et al.*: 'Novel fault location in MTDC grids with non-homogeneous transmission lines utilizing distributed current sensing technology', *IEEE Trans. Smart Grid*, 2017, Early Access Articles
- [6] Orr, P., Fusiek, G., Booth, C.D., *et al.*: Flexible protection architectures using distributed optical sensors'. 11th Int. Conf. Developments in Power Systems Protection, Birmingham, UK, April 2012, pp. 1–6
- [7] Orr, P., Fusiek, G., Niewczas, P., *et al.*: 'Distributed photonic instrumentation for power system protection and control', *IEEE Trans. Instrum. Meas.*, 2015, **64**, (1), pp. 19–26
- [8] Orr, P., Booth, C., Fusiek, G., *et al.*: 'Distributed photonic instrumentation for smart grids'. IEEE Int. Workshop on Applied Measurements for Power Systems, Aachen, Germany, Sept 2013, pp. 63–67
- [9] Fusiek, G., Orr, P., Niewczas, P.: 'Temperature-independent high-speed distributed voltage measurement using intensometric FBG interrogation'. IEEE Int. Instrumentation and Measurement Technology Conf., Pisa, Italy, May 2015, pp. 1430–1433
- [10] Orr, P., Fusiek, G., Niewczas, P., *et al.*: 'Distributed optical distance protection using FBG-based voltage and current transducers'. 2011 IEEE Power and Energy Society General Meeting, Detroit, MI, USA, July 2011, pp. 1–5
- [11] Niewczas, P., McDonald, J.R.: 'Advanced optical sensors for power and energy systems applications', *IEEE Instrum. Meas. Mag.*, 2007, **10**, (1), pp. 18–28
- [12] Callavik, M., Blomberg, A., Hafner, J., *et al.*: 'The hybrid HVDC breaker', in ABB Grid Systems, November 2012
- [13] Fusiek, G., Niewczas, P., McDonald, J.: 'Feasibility study of the application of optical voltage and current sensors and an arrayed waveguide grating for aero-electrical systems', *Sens. Actuat. A*, 2008, **147**, (1), pp. 177–182
- [14] Synaptec-Ltd: 'Our technology', <http://synapt.ec/our-technology>, accessed 15 November 2017